Chin. J. Astron. Astrophys. Vol. 5 (2005), No. 6, 645–664
(*http://www.chjaa.org*)

Chinese Journal of
Astronomy and
Astrophysics

A Multi-Wavelength Study of the 3B/X1.2 Flare Observed on 2003 October 26 *

Hui Li[1], Jian-Ping Li[2], Cheng Fang[2], Brigitte Schmieder[3,4], Arkadiusz Berlicki[3,5] and Qiu-Sheng Du[1]

[1] Purple Mountain Observatory, Chinese Academy of Sciences, Nanjing 210008; *lihui@mail.pmo.ac.cn*
[2] Department of Astronomy, Nanjing University, Nanjing 210093
[3] Observatoire de Paris, Section de Meudon, LESIA, F-92195, Meudon Principal Cedex, France
[4] Institute of Theoretical Astrophysics, University of Oslo, Blindern, N-0315 Oslo, Norway
[5] Astronomical Institute of the Wrocław University, ul.Kopernika 11, 51-622 Wrocław, Poland

Received 2005 May 9; accepted 2005 August 30

Abstract We report results from a multi-wavelength study of the 3B/X1.2 two-ribbon disk flare (S15E44), which was well observed by both ground-based and space-borne instruments. Two pairs of conjugate kernels – K1 and K4, and K2 and K3 – in the Hα images are identified. These kernels are linked by two different systems of EUV loops. K1 and K4 correspond to the two 17 GHz and 34 GHz microwave sources observed by the Nobeyama Radioheliograph (NoRH), while K2 and K3 have no corresponding microwave sources. Optical spectroscopic observations suggest that all the four kernels are possible precipitating sites of non-thermal electrons. Thus the energy of electron deposited in K2 and K3 should be less than 100 keV. Two-dimensional distributions of the full widths at half maximum (FWHM) of the Hα profiles and the line-of-sight (LOS) velocities derived from the Ca II 8542 Å profiles indicate that the largest FWHM and LOS velocity tends to be located near the outer edges of Hα kernels, which is consistent with the scenario of current two-ribbon flare models and previous results. When non-thermal electron bombardment is present, the observed Hα and Ca II 8542 Å profiles are similar to previous observational and theoretical results, while the He I 10830 Å profiles are different from the theoretical ones. This puts some constraints on future theoretical calculation of the He I 10830 Å line.

Key words: Sun: flares – Sun: X-rays – line: profiles

* Supported by the National Natural Science Foundation of China.

1 INTRODUCTION

As generally accepted, a solar flare happens when the free magnetic energy stored in a non-potential magnetic structure is suddenly released through some magnetic reconstruction, such as magnetic reconnection (Carmichael 1964). A variety of flare models have been established, as reviewed, for example, by Švestka & Cliver (1992), Priest & Forbes (1992) and Lin et al. (2003). Flare models in the past two decades have emphasized the relevance of chromospheric evaporation, which happens when the chromospheric plasma is heated to coronal temperature, resulting simultaneous downward motion of chromospheric plasma and upward motion of coronal material (Fisher 1987). The existence of chromospheric evaporation was confirmed by both observations (e.g., Antonucci et al. 1984; Schmieder et al. 1987, 1990; Teriaca et al. 2003) and numerical simulations (Yokoyama & Shibata 2001; Miyagoshi & Yokoyama 2004). According to the current two-ribbon flare model, as a flare goes on, successive energy conversion takes place at the magnetic reconnection site that keeps moving upward, which consequently causes the flare ribbons on the solar surface to separate and the flare loops in the corona to grow (e.g., Forbes & Acton 1996). This scenario of two-ribbon flare was supported by various observations, such as the loop-top HXR source as demonstrated in Masuda and RHESSI flares (see Masuda et al. 1994; Sui & Gordon 2003; Sui et al. 2004), the cusp structure in soft X-ray (SXR) (Tsuneta et al. 1992), and the increasing footpoint separation (Fletcher & Hudson 2001). Recently, it is realized that solar flare, eruptive prominence and coronal mass ejection (CME) may be different responses to the same catastrophic process in the corona and attempt was made to explain all these eruptive phenomena with one theoretical model (e.g., Forbes & Isenberg 1991; Forbes & Acton 1996; Shibata 1999; Lin & Forbes 2000; Lin 2004).

The released energy dissipates in the corona at and near the reconnection sites and subsequently leads to particle acceleration (Brown 1971), direct plasma heating (Brown et al. 1979), and plasma motion. Particle acceleration can be produced by various mechanisms and has been extensively studied (e.g., Litvinenko 1996; Miller et al. 1997; Priest & Forbes 2002). The released energy is transported to, and thus heats the chromosphere both non-thermally by the accelerated non-thermal particles (mainly electrons) and thermally by the evaporation, soft X-ray heating, cooling of hot coronal plasma by radiative losses, reconnection downflow, and thermal conduction(Schmieder et al. 1987, 1990; Forbes & Acton 1996; Yokoyama & Shibata 2001; Miyagoshi & Yokoyama 2004; Li et al. 2005a). This results in emissions in chromospheric lines, such as Hα, Ca II 8542 Å and He I 10830 Å.

These chromospheric lines show their specific sensitivities to various chromospheric heating mechanisms. Therefore, their spectroscopic behavior sometimes can be used to diagnose whether or not non-thermal electrons are present in the solar flare. Theoretical computations showed that the Hα line is most significantly affected by non-thermal electron bombardment (e.g., Canfield et al. 1984; Fang et al. 1993). In an atmosphere with non-thermal electron bombardment, the Hα line shows very broad profiles due to the Stark effect resulting from a significant increase of the electron number density, and strong central reversal due to the escape of photon in the upper atmospheric layers (Fang et al. 1993). Such profiles have been observationally reported (e.g., Ichimoto & Kurokawa 1984; Canfield et al. 1990). The Ca II 8542 Å line and other calcium lines, such as Ca II H and Ca II K, are less affected by bombardment of non-thermal electron beams, probably because these lines are formed at higher temperatures and layers (Fang et al. 1993, 2000). Non-LTE calculation also suggested that the He I 10830 Å line could be a potential diagnostic tool for non-thermal effects in solar flares because the presence of non-thermal electron beam can significantly increase the strength of He I 10830 Å emission in a hot atmosphere (Ding et al. 2005). Moreover, red asymmetries and red-shift velocities of chromospheric lines were frequently observed in the impulsive phase of solar flares (e.g.,

Tang 1983; Ichimoto & Kurokawa 1984; Canfield et al. 1990; You et al. 1993; Liu & Ding 2002; Teriaca et al. 2003), which are ascribed to the downward motion of chromospheric condensation driven by chromospheric evaporation due to non-thermal electron beam bombardment and/or thermal conduction, as well established by Fisher (1989).

The GOES SXR flux was observed to be correlated with the cumulative microwave flux (Neupert 1968) and with the cumulative time integral of the HXR flux (e.g., Brown 1971; Hudson 1972; Veronig et al. 2005; Li et al. 2005a) in the impulsive phase of solar flares. In other words, the differential GOES X-ray flux in the impulsive phase resembles the microwave flux and HXR flux. This is the so-called 'Neupert effect' (Hudson 1991), which provides evidence for a causal relationship between the non-thermal and thermal flare emissions – the SXR emission at a given time is related to the accumulated energy deposited by non-thermal electrons up to the given this time (e.g., Neupert 1968; Hudson 1972; Veronig et al. 2005).

Solar flares can enhance emissions in almost the whole electromagnetic wave range, from microwave to gamma rays, showing the importance and necessity of multi-wavelength studies of solar flares that have been widely undertaken (e.g., Canfield et al. 1990; Wülser et al. 1992; You et al. 1998; Ding et al. 2003; Li & Ding 2004; Li et al. 2005b). With the improved accuracy and resolution of various observational instruments, self-consistent synthetic multi-wavelength analysis of solar flares can provide more valuable information for understanding the physical process of solar flares. In this paper, we present results of a multi-wavelength study of the 3B/X1.2 two-ribbon disk flare of 2003 October 26. Studies of the associated coronal mass ejection, which was first detected around 06:54 UT, and the fine structures in microwave flux are described in other papers (Qiu et al. 2005; Ning et al. 2005). In Section 2, we will introduce our observations mainly in radio and optical ranges and our data analysis. We will describe our results in Section 3, and give a discussion and the conclusions in Section 4.

2 OBSERVATIONS

This flare was observed by several ground-based instruments, including the Multi-channel Infrared Solar Spectrograph (MISS) at Purple Mountain Observatory (PMO) (Li et al. 1999, 2002), the imaging solar spectrograph (ISS) in the Solar Tower of Nanjing University (NJU) (Huang et al. 1995; Ding et al. 1999), the Nobeyama Radioheliograph (NoRH) (Nakajima et al. 1994), and the Solar Broadband Radio Spectrometer (SBRS) (Fu et al. 1995) at Huairou Solar Observation Station (HSOS) of National Astronimical Observatories of China (NAOC).

The MISS observation began at 05:59 UT and ended at 08:02 UT, covering the whole flaring process. The observational data consist of spectra of three lines – Hα, Ca II 8542 Å and He I 10830 Å – and Hα images obtained simultaneously with the spectra by the slit-jaw system, which uses a Daystar filter with 0.5 Å passband. The integration times of the Hα, Ca II 8542 Å and He I 10830 Å spectra are, respectively, 0.06 s, 0.06 s and 0.4 s, and the spectral dispersions are 0.05453 Å, 0.05113 Å and 0.04776 Å per pixel, respectively. The spatial resolution is 1.34″ along the slit after 4-row binning. The spectral data were first corrected for dark-current, flat-field, scattering light and instrument profile, and then absolutely calibrated by using the continuum intensity near these wavelengths. The calibration was done by comparing the observed profiles in a nearby quiet region with theoretical mean profiles for Hα (David 1961) and Ca II 8542 Å (Linsky et al. 1970), and with an observed standard profile for He I 10830 Å (http://bass2000.obspm.fr/).

ISS observes the Sun in Hα and Ca II 8542 Å lines. We have obtained a time series of two dimensional (2D) spectra in the Hα and Ca II 8542 Å lines. The 2D spectroscopic observation is realized by scanning, i.e., moving the solar image across the slit of the spectrograph with a step of about 2″. ISS completes a scan of 50 steps in about 18 s, including the time to move

the image back to the initial position. The ISS observations for this flare began at 06:04:33 UT and ended at 07:09:16 UT, covering most of the impulsive and gradual phase of the flare. A total of 39 frames of 2D Hα and Ca II 8542 Å spectra were recorded. There are 120 pixels with a spacing of 0.85″ along the slit and 50 pixels with a spacing of 2″ in the scan direction. The spectrum contains 260 wavelength points with a spectral resolution of 0.050 Å and 0.118 Å per pixel for the Hα and Ca II 8542 Å lines, respectively. The data reduction includes dark current subtraction and the flat-field correction for the CCD camera. The drift of images at different times is also corrected by carefully co-aligning the sunspot locations in these images. The centers of the Hα and Ca II 8542 Å lines are determined from the mean undisturbed profiles near the flare region by Gaussian fitting. We can reconstruct a monochromatic image at the line center and in the line wing of Hα and Ca II 8542 Å for each scan in the following way. We take one column from each spectrogram of a scan series and put it in a column of the new image in the same order as the scan. The reconstructed image at this step has pixel sizes of 2″ and 0.85″ in X- and Y-direction, respectively. Then the image is rebinned so that it has equal pixel size along the two axes.

NoRH is a solar radio telescope dedicated to full-disk observations. It observes the Sun at 17 GHz in both right- and left-circular polarizations and at 34 GHz in intensity, with spatial resolutions of about 4.9″ /pix at 17 GHz and 2.45″ /pix at 34 GHz, respectively, and with the time resolution of 1 s. In this paper, we use the flux-curves and images at both 17 GHz and 34 GHz. SBRS provides flux curves at 1.42 GHz, 2.84 GHz and 5.70 GHz.

This flare was also observed by some space-borne instruments, including the Geostationary Operational Environmental Satellites (GOES), the Solar and Heliospheric Observatory (SOHO) (Domingo et al. 1995) and the Transition Region and Coronal Explorer (TRACE) (Handy et al. 1999). The X-ray data are from GOES and the magnetic field data from SOHO/MDI. TRACE observed this flare in 195 Å and 1600 Å with a cadence of about 12 seconds during the impulsive phase, which provided the EUV data used in this paper.

3 RESULTS

3.1 Flare Evolution

The Solar Geophysical Data (SGD) register indicates that the X-ray flare started at 05:57 UT, peaked at 06:54 UT and ended at 07:33 UT. We plot the GOES X-ray flux time profile in Figure 1(a), and radio flux time profiles from SBRS in Figure 1(b). Figure 1(a) shows that the X-ray emission underwent a multi-stage evolution, which presumably suggests multiple magnetic reconnections in the course of the flaring. After its first increase, the GOES X-ray flux kept almost constant during the period from 06:00 UT to 06:08 UT; it then started to increase impulsively and reached its first peak at about 06:19 UT. The X-ray flux remained at a high level with a slight decrease and then once again increased to its second peak at 06:54 UT. The radio emission (Fig. 1(b)) displayed corresponding changes but not as impulsively and intensively as did the X-ray emission. The radio flux-curves showed multiple peaks and peaked around 07:30 UT. These multiple peaks are discussed in another paper (Ning et al. 2005). In this paper, we will limit our study to the period before 06:30 UT (i.e., mainly in the impulsive phase) and will discuss in detail the time flux curves in Section 3.4.

We display nine normalized Hα images obtained by the slit-jaw system of MISS in Figure 2, which shows the flare′s evolution in Hα. The black straight lines in Figure 2 are the entrance slit of the spectrograph. There was already an Hα kernel at 05:59:10 UT (Fig. 2(a)), which slowly increased its area and developed into a pair of weak ribbons until 06:03:07 UT (Fig. 2(b)–(c)); then the flare evolved into a typical two-ribbon flare at 06:10:45 UT (Fig. 2(d)). The two ribbons

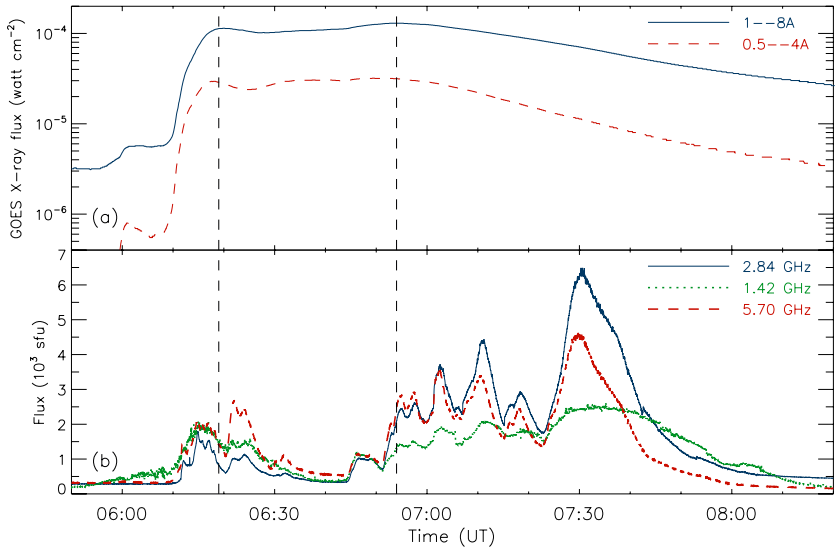

Fig. 1 (a) GOES X-ray flux in 1–8 Å and 0.5–4 Å wavebands; (b) Radio flux at 1.42 GHz (dotted), 2.84 GHz (solid) and 5.70 GHz (dashed) from the SBRS at HSOS, NAOC. The two dashed vertical lines indicate the two peak times of GOES 1–8 Åflux.

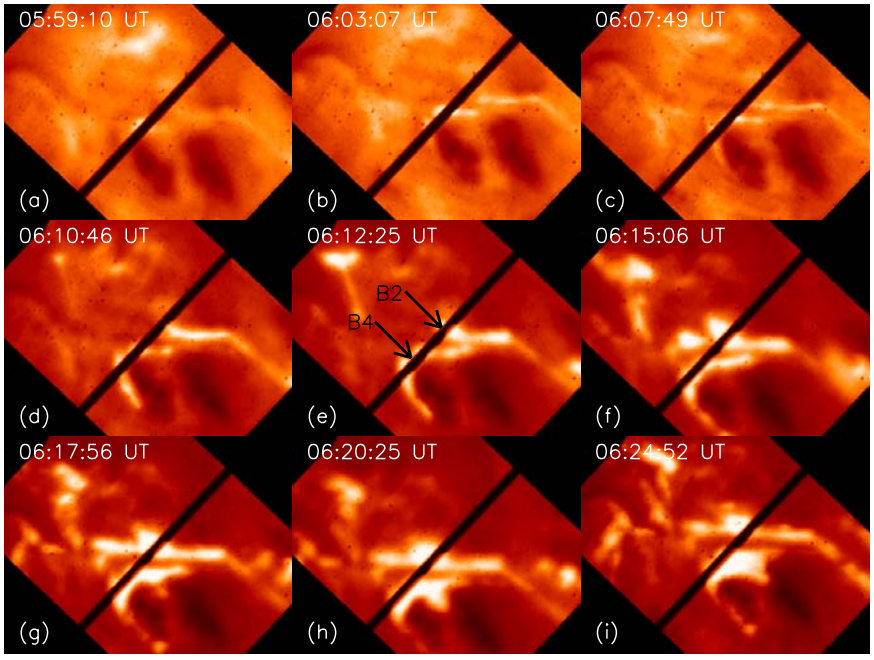

Fig. 2 Selected slit-jaw Hα images obtained by the MISS at PMO. The observation times are indicated in each image. The image size is 191″ × 143″. North is on the top and east to the left. We will keep to this convention for all images in this paper. The black straight lines are the entrance slit of the spectrograph. B2 and B4 are two points located in the bright parts of kernels K2 and K4, respectively, which are discussed in Sect. 3.2.

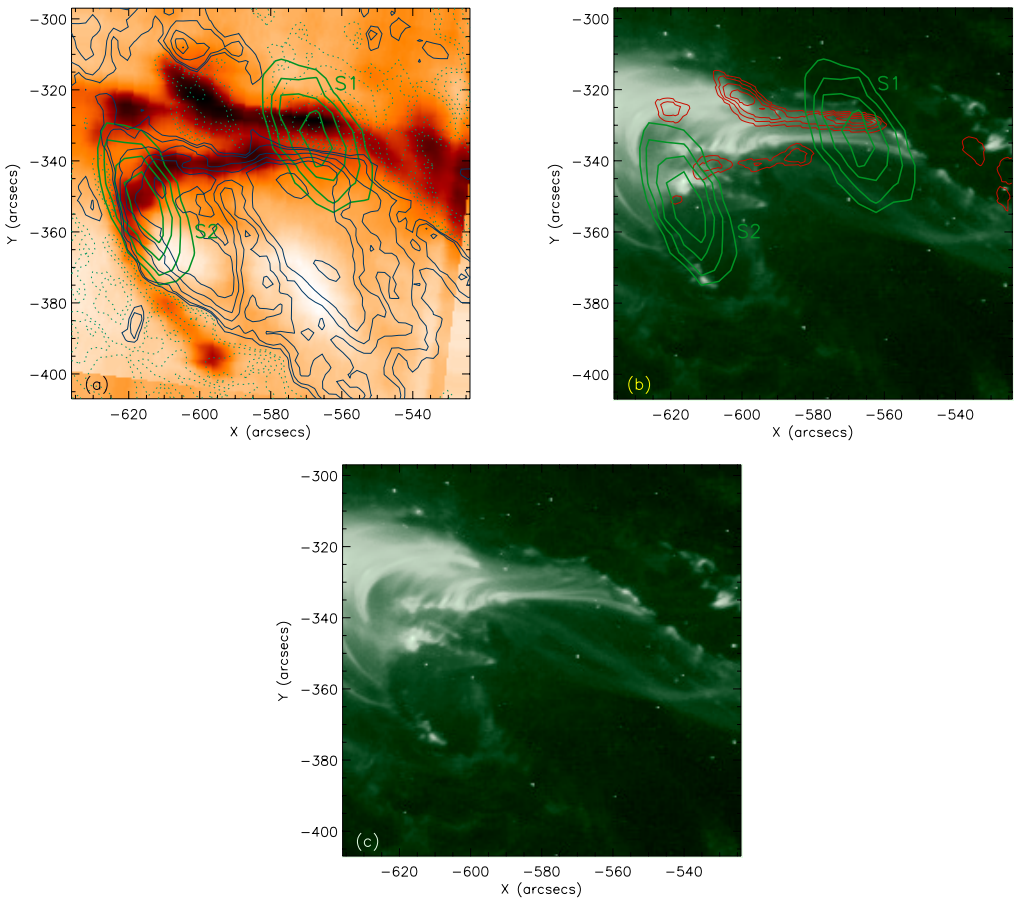

Fig. 3 (a) NoRH 17 GHz image at 06:11:49 UT (white contour) and longitudinal magnetic field (black contour) from SOHO/MDI are superposed on the reconstructed Hα image at 06:14:48 UT from ISS. (b) ISS Hα image at 06:14:48 UT (thin contour) and NoRH 17 GHz image at 06:11:49 UT (thick contour) are superposed on the TRACE/195 Å image at 06:24:34 UT. (c) TRACE/195 Å image at 06:24:34 UT showing clearly the loop systems. 'S1' and 'S2' in (a) and (b) indicate the two 17 GHz radio sources. The contour levels for the Hα image are 60%, 70%, 80%, and 90% of the maximum intensity, those for the 17 GHz image are 60%, 70%, 80%, and 90% of the maximum flux, and those for the magnetic fields are $\pm$(100, 200, 400, 600, 800, 1200, 1600) G. The solid and dotted thin contours indicate the positive and negative magnetic polarities, respectively.

brightened and enlarged in the ensuing time with the formation of several kernels (see Sect. 3.2 for details).

We coaligned the Hα image, SOHO/MDI magnetogram, TRACE 195 Å image and NoRH radio image in Figure 3. The two Hα ribbons are located in opposite magnetic polarities (Fig. 3(a)) and are the footpoints of the EUV loops (TRACE image). The loops connect the two radio sources at 06:11:49 UT (Fig. 3(b)). Figure 3 also shows that the radio sources are shifted to the south-east with respect to the Hα ribbons, which could be explained by projecting effects, bearing in mind that the flare is located at S15E44.

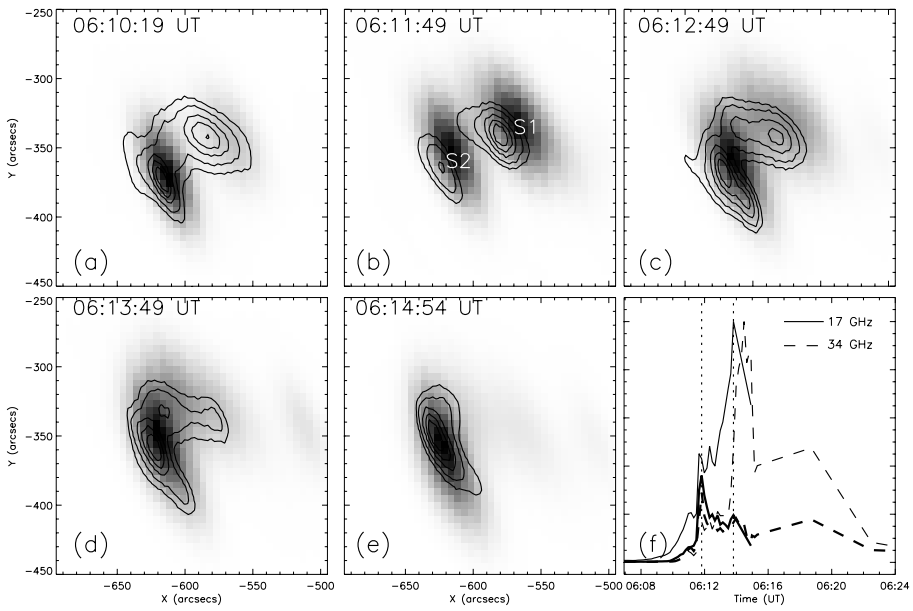

Fig. 4 NoRH 34 GHz images (contour) are superposed on NoRH 17 GHz images at (a) 06:10:19 UT, (b) 06:11:49 UT, (c) 06:12:49 UT, (d) 06:13:49 UT and (e) 06:14:54 UT. The observation times are shown in each image. The contour levels are 10%, 20%, 40%, 60%, and 80% of the maximum value of each image. (f) Flux-curves for radio sources S1 (thick) and S2 (thin) from NoRH at 17 GHz (solid) and 34 GHz (dashed).

We present five selected microwave images of this flare obtained by NoRH at 17 GHz (background) and 34 GHz (contour) in Figure 4. There were two asymmetric radio sources, S1 and S2, in the early phase before 06:13 UT (Fig. 4(a)–(c)). S1 weakened at 06:13:49 UT and disappeared after 06:14 UT. The light-curves of these two sources are plotted in Figure 4(f). Source S1 reached its maximum brightness around 06:11:49 UT, corresponding in time to the first peak of the differential GOES X-ray flux and radio flux (see Sect. 3.4 for details); while the brightness of S2 peaked around 06:13:49 UT, corresponding to the second peak of the differential GOES X-ray flux and radio flux. Therefore, we can infer that both S1 and S2 contribute to the radio flux before 06:13 UT, while afterwards the flux are mainly from the source S2.

It is noticed from Figure 4 that the 34 GHz radio sources are shifted to south-east with respect to the 17 GHz sources. This is likely not a true shift. NoRH is a radio interferometer. The phase and amplitude calibrations are one of the most difficult tasks when acquiring high quality images. Its positioning accuracy depends on the determination of the quiet Sun in the synthesized image. If the quiet Sun is well defined in the synthesized image we can obtain high positional accuracy. On the other hand, the positional accuracy is not high enough if the quiet Sun is not well defined due to very bright sources on the Sun, which is often the case during very strong flares (Shibasaki, private communication). For the flare under study, the flare contributions to the microwave flux at both 17 GHz and 34 GHz well exceed 1000 sfu, which is much larger than the integrated quiet Sun flux ($\sim$ 600 sfu). So, it is necessary to assume that the positional accuracy is not high, which could lead to the relative displacements shown in Figure 4 between the 17 GHz and 34 GHz sources. In our case, the 17 GHz flux is lower

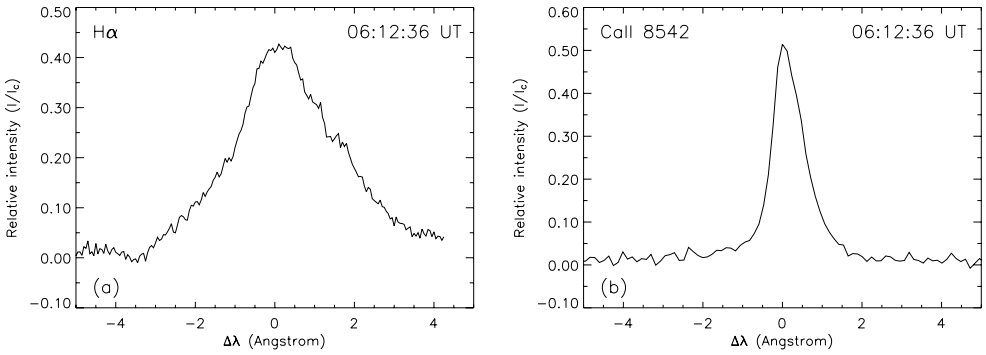

Fig. 5 Example of (a) Hα and (b) Ca II 8542 Å excess profiles observed by ISS at 06:12:36 UT. The intensity is scaled by the continuum, I_c, in a nearby quiet region.

than 34 GHz flux, suggesting that the position information from 17 GHz images may be more reliable.

3.2 Velocities and FWHM of the Flare Plasma in the Ribbons

Using the ISS 2D spectral data, we have derived maps of intensity, line-of-sight (LOS) velocity and FWHM. We reconstructed monochromatic images at the center and in the wings of the Hα and the Ca II 8542 Å lines (see Sect. 2 for details).

The LOS velocity is derived from far wings (at 5% of the peak intensity) of the excess profiles (with a pre-flare profile subtracted) using a bisector method (Ding et al. 1995) which roughly reflects still the dynamics in the chromosphere. During the observation of the flare, the Hα spectral window had a departure of 44 wavelength points from the line center, so the far red wing of the Hα profiles within the range of interest was outside of the observation window. Consequently, the observed Hα profiles are not suitable for calculating the LOS velocities using the wing bisector method (see examples of the Hα and the Ca II 8542 Å profiles in Fig. 5). However, this departure has no much influence on the calculation of the FWHMs. Therefore, we use the Hα profiles to deduce the FWHMs and the Ca II 8542 Å profiles for the LOS velocities.

Monochromatic images at the Hα line center at six times selected from the whole set of 39 frames and covering the times of the two peaks of the differential GOES X-ray flux and radio flux were reconstructed from the ISS spectra. They are overlaid by the 2D distributions of the velocity fields deduced from the Ca II 8542 Å profiles (Frames (a)–(f) in Figure 6). The Hα and the Ca II 8542 Å data are recorded simultaneously and we have made a careful coalignment between the Hα images and the Ca II 8542 Å images using a cross-correlation method. The correlation is expected to be good to about 2 arc sec in each direction. Throughout the development of the flare, we identified four kernels (labelled 'K1', 'K2', 'K3', and 'K4' in Fig. 6(c)) in the Hα line-center monochromatic images that have different features in the velocity distributions.

The line of sight velocities are computed by the bisector method. It is generally a good proxy for the Doppler shifts when the background is well defined, and this is the case for kernels K1, K2, and K4. For kernel K3 the background is the penumbra of a sunspot and is difficult to estimate. A complete study of radiative transfer should be applied to derive correctly the velocities. Nevertheless, we have obtained during the impulsive phase in the kernels some flows of maxima reaching 30 to 40 km s^{-1} . It is consistent with previous studies. The 2D maps

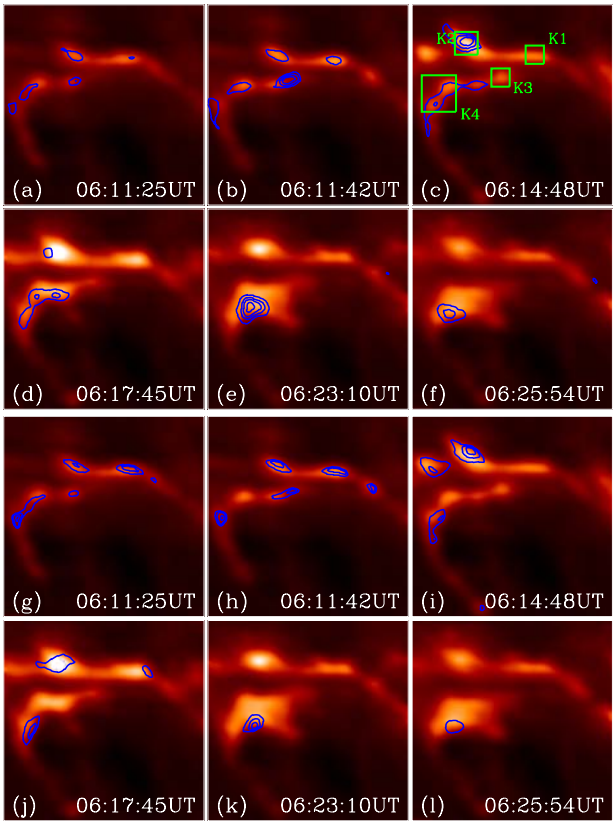

Fig. 6 Hα line-center images overlaid by contours of the LOS velocities (the two upper rows, Frames (a)–(f)) and by contours of the FWHMs (the two lower rows, Frames (g)–(l)) derived from the ISS 2D spectroscopic observations in Ca II 8542 Å and Hα, respectively. The contour levels are –(12, 19, 26, 33) km s^{-1} ('–' stands for red-shift velocity) for the LOS velocities and (1.9, 2.3, 2.7, 3.0) Å for the FWHMs, respectively. The observation time is shown in each image. The image size is 80″ ×80″ .

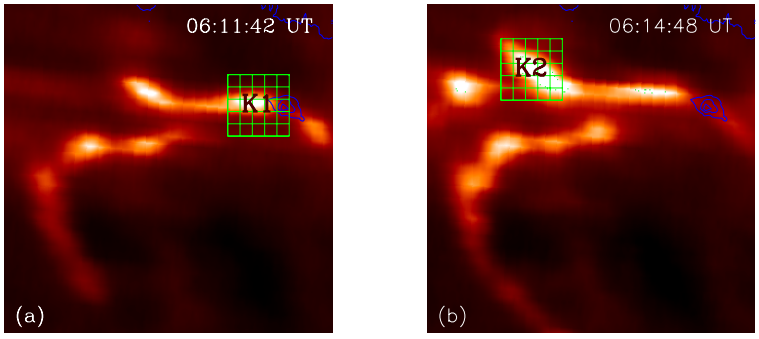

Fig. 7 Reconstructed Hα images showing the grids in which the Hα profiles are retrieved and plotted in Figs. 8 and 9. The contours mark the Hα–1.0 Å kernels at 06:10:10 UT with contour levels of 0.9, 0.95 and 0.98 of the maximum image value. The observation time is shown in each image. The image size is 80″ ×80″ .

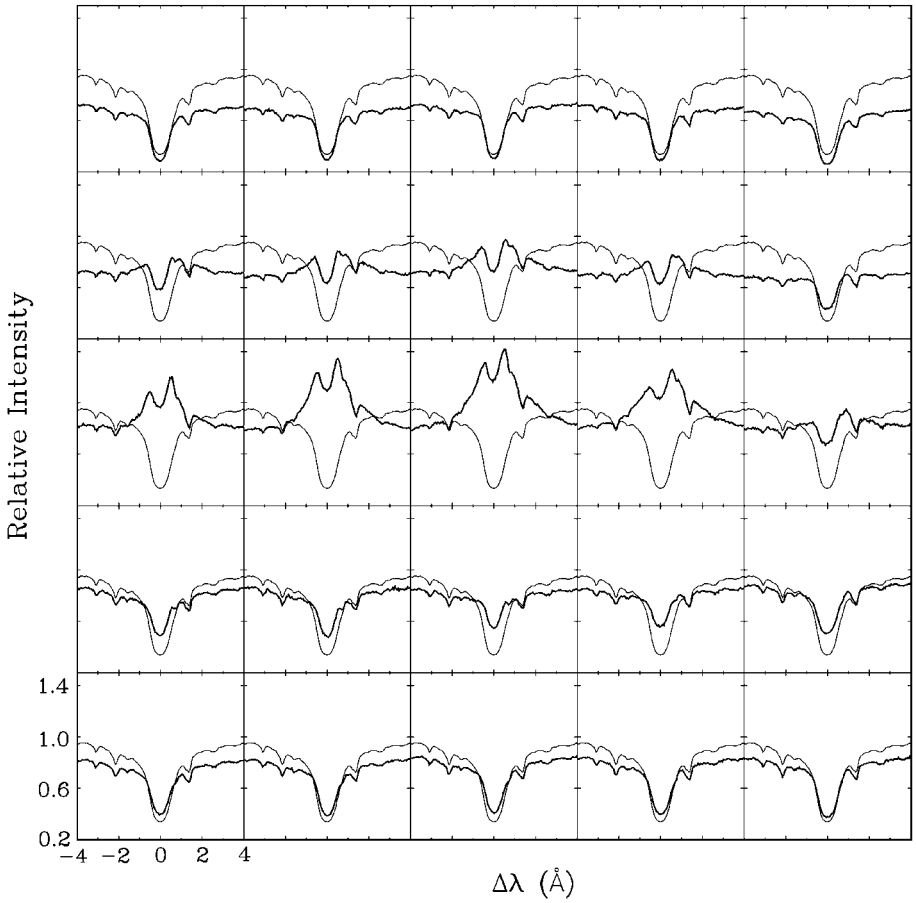

Fig. 8 Retrieved Hα profiles (thick lines) at 06:11:42 UT for kernel K1 (see Fig. 6(c)) in the grid area in Fig. 7(a) and for a nearby quiet region (thin lines).

of downflows indicate that the largest ones are on the outer edge of the ribbons. Two impulsive pulses were registered in the time curves (radio and optical). Multiple reconnections occur in this flare, one corresponding to a velocity maximum in kernel K3 at 06:11:42, the other, in the kernel K2 at 06:14:48 UT. In addition, it seems that the centroids of the velocity field and the line-center brightness do not coincide at any of the times for each kernel, except kernel K3. Very often the brightest pixels at line center do not exhibit the strongest velocity and, conversely, pixels with larger velocities are often of only modest brightness at the line center and tend to be located on the outer edges of the bright kernels.

Frames (g)–(l) in Figure 6 show the 2D distributions of the FWHMs deduced from the Hα profiles, superposed on the Hα monochromatic images, like the velocity distributions described above. Through a detailed comparison, we found that the FWHM kernels spatially correspond to the velocity kernels. Therefore, the distribution of FWHMs has similar features to that of the LOS velocities. For example, large FWHMs are detected at kernel K3 around 06:11:42 UT and at kernel K2 around 06:14:48 UT, temporally corresponding to the first and second peaks of the differential GOES X-ray flux and radio flux, respectively; the maximum values of FWHMs also tend to occur on the outer edges of the brighter kernels.

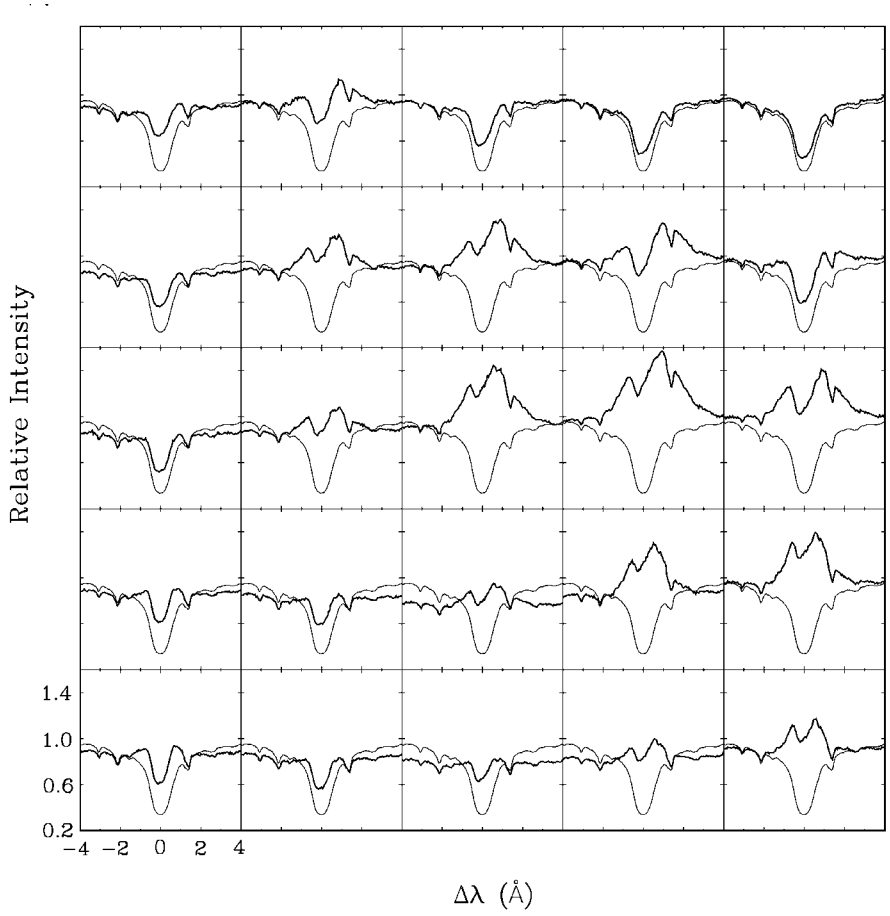

Fig. 9 Retrieved Hα profiles (thick lines) at 06:14:48 UT for kernel K2 (see Fig. 6(c)) in the grid area in Fig. 7(b) and for a nearby quiet region (thin lines).

3.3 Analysis of Spectral Profiles

Theoretical studies have shown the effect of bombardment of non thermal particles on the shape of chromospheric line profiles (e.g., Fang et al. 1993, 2000). Emission profiles with apparent non-thermal effect are characterized by greatly broadened wings and obvious central reversals. To explore the features of line profiles and search for emission profiles with apparent non-thermal effect, we draw the Hα profiles in the two grid areas overlaid on the kernels K1 and K2 (Fig. 7) at 06:11:42 UT and 06:14:48 UT, respectively, in Figures 8 and 9.

K1 is relatively compact compared with K2. Only the center part of K1 shows emission profiles, and in the upper (north) and lower (south) parts of K1, the Hα profiles are similar to those in the quiet region (Fig. 8, the first and the last rows). All the emission Hα profiles in Figure 8 show red asymmetries and central reversals, but they do not apparently show broad wings. We use two digits in square brackets to specify the location of a profile in the grid in Figures 8 and 9: for example, [2,3] stands for the profile retrieved for the grid in the second row and the third column. If we just look at the profiles, then even the widest profile with the strongest emission (Fig. 8 [3,3]) has no obvious emission in the far wings ($\Delta\lambda > 2$ Å) of Hα.

However, kernel K1 is located in a sunspot and its pre-flare continuum should be less than in a nearby quiet-Sun region. If we take this fact into account, the strong profiles then show emissions in the far wings, although they are different from previous observed profiles showing effect of non-thermal electron bombardment (Canfield et al. 1984; Ichimoto & Kurokawa 1984). Therefore, we could say that there exists non-thermal effect in kernel K1 at 06:11:42 UT even though it is not as remarkable as in kernel K2 described below.

Red asymmetrical emission profile was observed in all the K2 grids, and all the profiles in the brighter (central) part have central reversal (see Fig. 9). The profiles in the middle-right part show non-thermal features (Figs. 9 [2, 4], [2, 5], [3, 4], [3, 5], [4, 4] and [4, 5]). The grids where the Hα profiles show the most significant non-thermal features (Figs. 9 [3, 4] and [3, 5]) spatially correspond to the north-west edge, rather than the center, of K2, suggesting that the non-thermal electrons precipitate at the outer edge of the Hα kernel. This is consistent with the predictions of the magnetic reconnection models and with other observations (e.g Falchi et al. 1997; Li & Ding 2004).

ISS provides for us 2D spectra that allow us to study the spectroscopic properties of the whole flaring area at a given time with time resolution of $\sim$ 18 s, while MISS provides spectral data for a fixed slit position with a relatively higher time resolution ($\sim$ 2.8 s). During MISS observations, the observer may put the slit at different positions of the flare by shifting the solar image. Using the SOHO/MDI intensity image as an intermediary, we can follow a point of interest by carefully coaligning the MISS slit-jaw Hα images to each other. In order to investigate the spectroscopic evolution, we selected spectra for two points marked 'B2' and 'B4' in Figure 2(e), which are two points located in the bright parts of kernels K2 and K4 (Fig. 6), respectively.

The Hα, Ca II 8542 Å and He I 10830 Å profiles for point B2 are plotted in Figure 10. From the figure we notice that the three lines have different features. All the Hα profiles displayed apparent central reversal, while no central reversal was observed in the Ca II 8542 Å and the He I 10830 Å profiles. Moreover, all the Ca II 8542 Å profiles are narrower than the Hα and He I 10830 Å profiles. At 06:10:46 UT when B2 just began to brighten, its Hα and Ca II 8542 Å profiles displayed emissions less than the continuum while the He I 10830 Å profile did not show any emission at all (Fig. 10, the first row). Furthermore, as its brightening area increased rapidly, the profiles at 06:12:25 UT in all the three lines became rather wide, red asymmetric and red-shifted (Fig. 10, the second row). The Hα profile is a typical non-thermal profile with deep central reversal and wide emission wings. Such profiles were observed in the period from 06:11:53 UT to 06:12:28 UT, implying the bombardment of non-thermal electron beams lasted at least 35 seconds. Its first appearance temporally corresponds to the first peak of differential GOES X-ray flux, and SBRS and NoRH radio fluxes (Fig. 13(b)). The Ca II 8542 Å profile was red asymmetric but not wide due to the small impact of the non-thermal electron beams on Ca II 8542 Å profiles (Fang et al. 2000). The He I 10830 Å profile at this moment was different from those at other times (see the middle column of Fig. 10 for details): we cannot distinguish the I_3 component (10829.081 Å) from the I_{12} component (10830.341 Å+10830.250 Å), indicating a large Doppler width (You et al. 1998; Li & You 2001). It is also different from the profile of the theoretical computation (Ding et al. 2005). In the He I 10830 Å profiles at other times, the I_{12} and I_3 components are clearly distinguishable. Later on, the emission of B2 in all the three lines continued to increase for several minutes and then decreased. At 06:24:52 UT, the He I 10830 Å line had almost no emission while the Hα and the Ca II 8542 Å lines showed still some weakened emissions.

The Hα, Ca II 8542 Å and He I 10830 Å profiles for point B4 are plotted in Figure 11. All the profiles in this figure exhibited similar features as in Figure 10 for point B2, such as a red asymmetry without wide emission wings in all the profiles, thus no signature of significant

non-thermal effect. Meanwhile, emissions in all the three lines were weaker than for the profiles at point B2. The Hα profiles after 06:15:06 UT (Fig. 11, left column, last two plots) showed a saturated line core, implying large optical thickness for the Hα line, while the Ca II 8542 Å and the He I 10830 Å profiles did not display any of that.

3.4 Time Profiles

From the selected Hα, Ca II 8542 Å and He I 10830 Å profiles for points B2 (in the kernel K2) and B4 (in K4), we derived the FWHMs and the LOS velocities at different observation times. We cannot use the bisector method to determine the LOS velocity from the He I 10830 Å profile, because it is a triplet and the wings of the three components overlap each other. To obtain the parameters, we first calculated the excess profiles by subtracting a pre-flare profile from the observed flare profiles and then simply used Doppler broadening to simulate the observed excess profiles, which yields the Doppler widths and the LOS velocities, even though the Doppler broadening may not be the actual broadening mechanism for these profiles. Then we acquired FWHMs by multiply the Doppler widths by a factor of $2\sqrt{\ln 2} = 1.665$. It is worth mentioning that the FWHMs of the He I 10830 Å profiles deduced in this way are not the real widths of the three-component profiles but the widths of one component (Li & You 2001; Li et al. 2005b). When simulating the He I 10830 Å excess profile, we supply the Doppler width of one component, the whole width of the simulated profile is calculated by a formula given in Li & You (2001) and Li et al. (2005b). The accuracy of the LOS velocity measured in this way is determined by the selection of reference line center, the derivation of the excess profiles and the fitting itself. The estimated accuracy is $3 - 5$ km s^{-1} for the LOS velocities measured from the Hα and the Ca II 8542 Å profiles, and $5 - 7$ km s^{-1} from the He I 10830 Å profiles.

The inferred FWHMs and LOS velocities are presented in Figure 12. The figure shows that both the FWHMs and the LOS velocities peaked around 06:12 UT and these parameters for B2 exhibit a more impulsive feature (changed more rapidly before the maximum), which is consistent with the bombardment of non-thermal electron beams at B2. The FWHMs of the Hα profiles underwent a rapid increase during 06:11:30 – 06:12:00 UT (Fig. 12(a)), temporally corresponding to the first peak of the microwave fluxes and the differential GOES X-ray flux. The LOS velocities are almost always negative (Fig. 12(b)), indicating red-shifts. This is consistent with the ISS observations even though they have lower values.

To compare the temporal evolutions of the GOES X-ray and the radio emissions with other parameters, such as, the Hα kernel brightness and the FWHMs of the line profiles, we plot in Figure 13 the GOES X-ray flux (Fig. 13(a)), the microwave/radio flux-curves and the differential GOES X-ray flux over a shorter time interval (05:50 UT – 06:50 UT) (Fig. 13(b)). Also plotted in Figure 13 are the time profiles of the FWHMs of Hα profiles for the selected areas (Frame (c)) and the brightness of the selected Hα kernels (Frame (d)), derived respectviely from the ISS Hα spectra and the reconstructed Hα images.

Figure 13(b) shows that the differential GOES X-ray flux is strongly correlated with the flux-curves at 5.70 GHz and 17 GHz, indicating that the Neupert (Neupert 1968) effect is present in this flare. The first peak of differential GOES X-ray flux matches well in time with the first peak of the microwave flux, while the other peaks of the microwave flux are more or less delayed with respect to the peaks in the differential GOES X-ray flux.

The FWHMs of the Hα profiles (Fig. 13(c)) and the time profiles of the brightness at Hα+1.5 Å (Fig. 13(d)) for the four kernels (Fig. 6) also have a good correlation with the differential GOES X-ray flux and the microwave flux-curves, suggesting that the impulsive increases in the FWHMs of the Hα profiles in the period around 06:10 UT to 06:12 UT are most probably caused by the bombardment of non-thermal electron beams, which leads to increase of the excitation and ionization of the hydrogen atoms, and hence the microturbulence. Contrary to

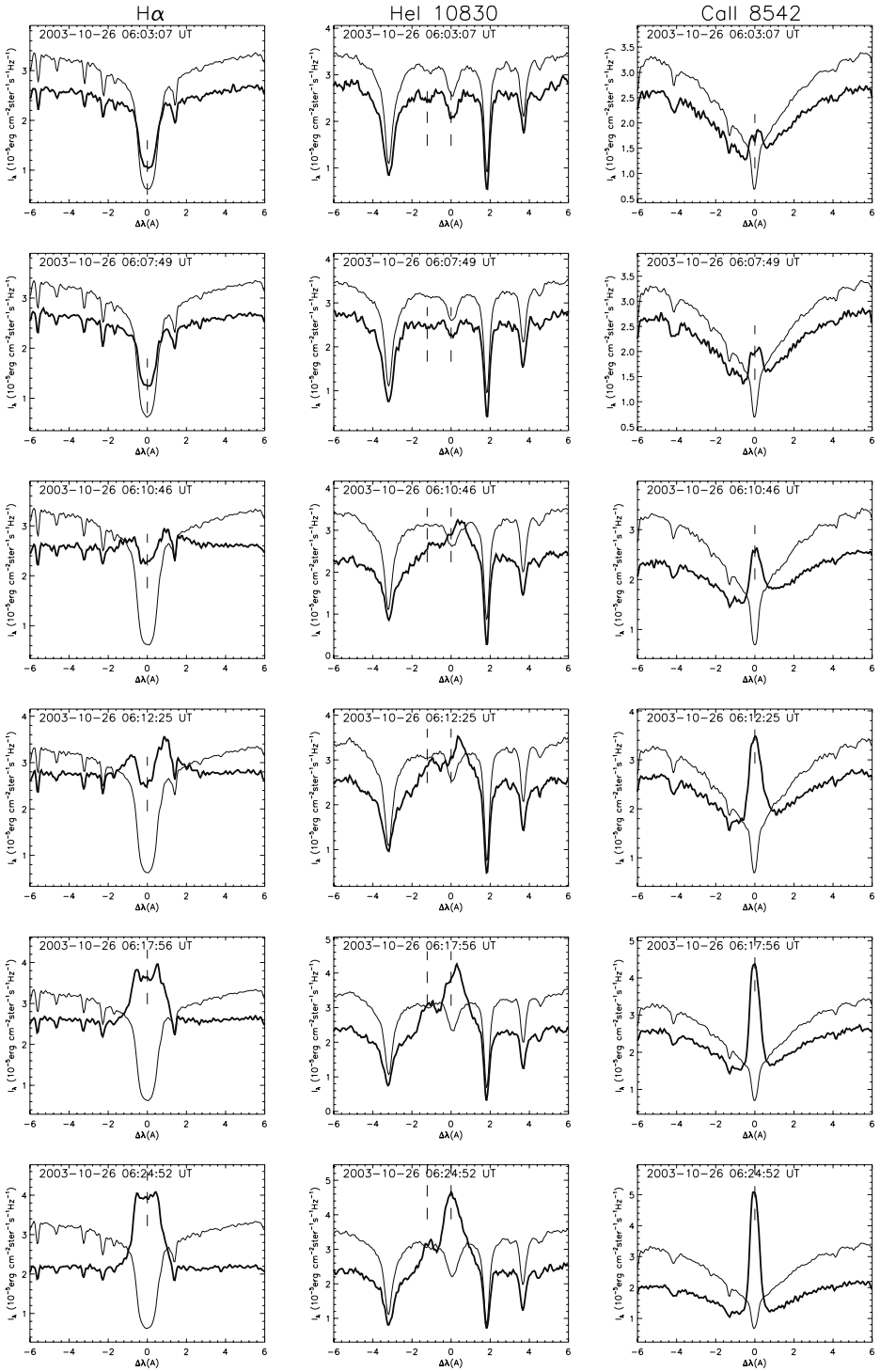

Fig. 10 Selected Hα (left), He I 10830 Å (middle) and Ca II 8542 Å (right) profiles (thick lines) of point B2 marked in Fig. 2(e) by an arrow, temporally corresponding to the Hα images shown in Fig. 2(d)–(i). The thin lines are the profiles of a nearby quiet region. The dashed vertical bars indicate the unshifted line-centers.

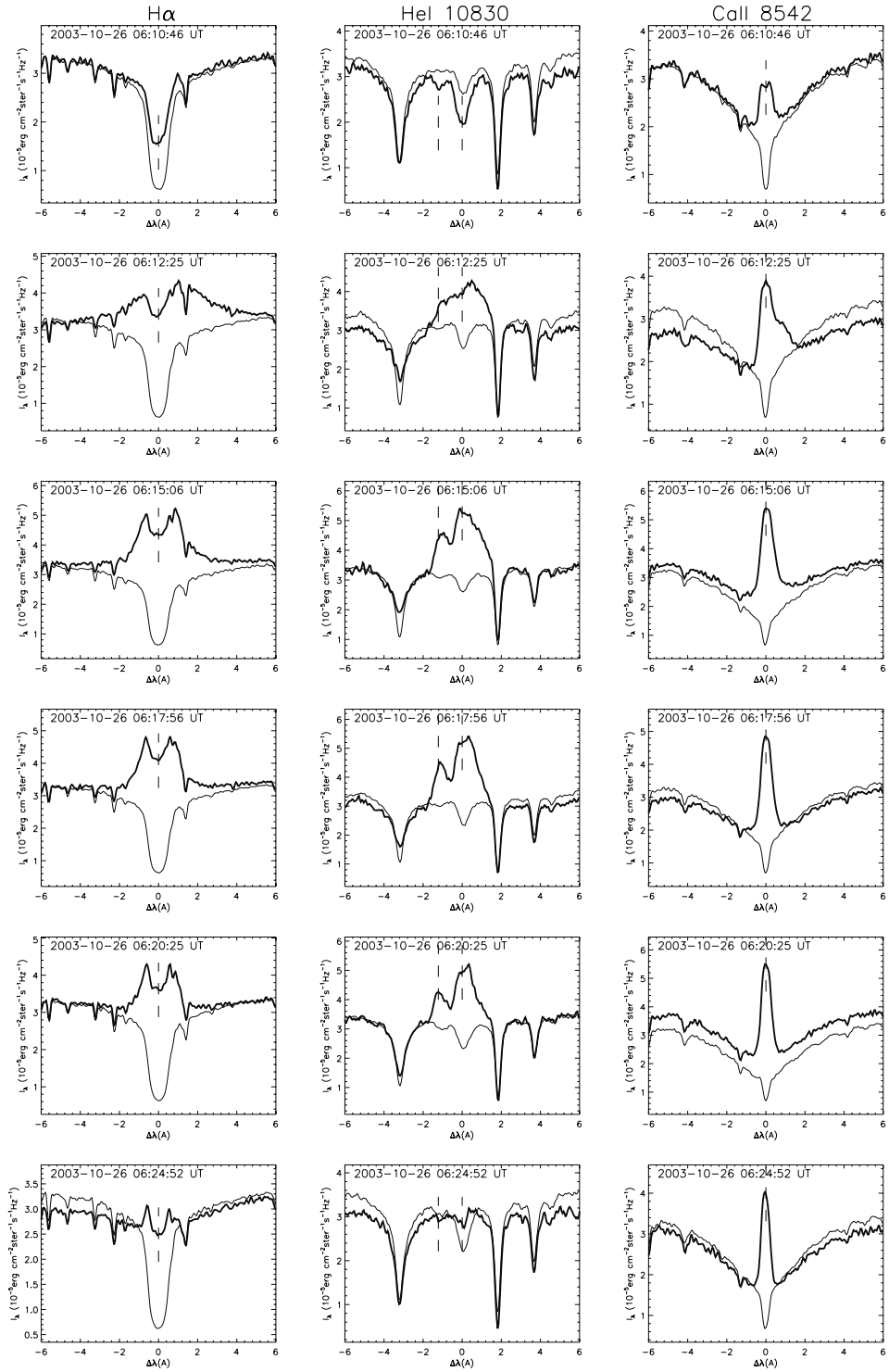

Fig. 11 Same as Fig. 10 but for point B4 and corresponding to the Hα images shown in Fig. 2(b), (c), (d), (e), (g) and (i).

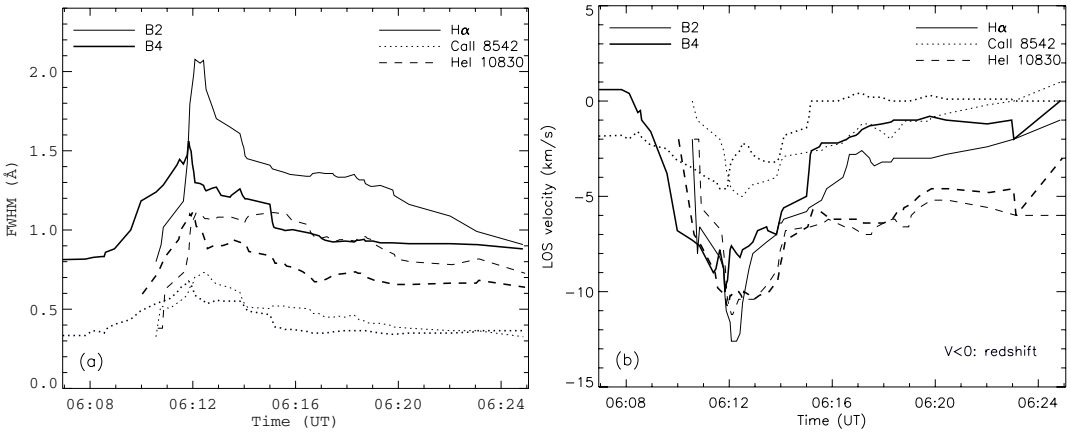

Fig. 12 Time profiles of (a) FWHMs and (b) LOS velocities derived from the Hα (solid), Ca II 8542 Å (dotted) and He I 10830 Å (dashed) profiles obtained by the MISS for point B2 (thin) and B4 (thick). Negative velocity represents red-shift. The estimated error of the LOS velocities from Hα and Ca II 8542 Å profiles is $3-5$ km s^{-1} , and that from He I 10830 Å profiles is $5-7$ km s^{-1} .

the increase, the FWHMs decreased rather gradually after reaching the maximum values. We saw that the FWHM increases at kernels K2 and K3 are delayed by about 1 minute compared with K1 and K4. However, the FWHMs for K1 and K4 varied synchronously, while those of K2 and K3 changed simultaneously. The brightness time profiles evolved similarly to the FWHMs as a whole, but their increases were not as impulsive as the FWHMs. These together with their morphological evolutions in the Hα images suggest that K1 and K4, and K2 and K3, are two pairs of conjugate kernels (cf. Figs. 2, 3 and 6).

We also derived the average LOS velocities for the four kernels from the ISS Ca II 8542 Å spectra. All the derived velocities indicate red-shifts. The red-shift velocities varied from a few to about 30 km s^{-1} in the impulsive phase (Figs. 6(b) and (c)) and around the flare peak time (Fig. 6(e)), which is consistent with the velocities derived from the MISS spectra shown in Figure 12. The temporal evolutions of the LOS velocities for the four kernels are similar to that of FWHMs, so we did not plot them in Figure 13.

4 DISCUSSION AND CONCLUSIONS

The analyzed 3B/X1.2 flare is a typical two-ribbon flare consisting of several Hα kernels, among which we selected four for study in this paper (K1, K2, K3, and K4). The coalignments of the magnetogram and the EUV image indicate that the two ribbons, as expected, are located in regions of opposite magnetic polarities and are the footpoints of EUV loops. The two microwave sources detected in the NoRH 17 GHz and the 34 GHz images (Fig. 4) evolved asymmetrically, and spatially corresponded to the Hα ribbons: S1 to K1 and S2 to K4. Microwave radiation at source S2 is, as a whole, stronger than at S1, but changes more gradually. This is probably because the reconnection sites are closer to S2 or because of the magnetic mirror effect that was first studied by Melrose & White (1979) and then by Sakao et al. (1996), and was applied to interpret the asymmetry of flare ribbons in different magnetic polarities (e.g., Li et al. 2000; Li & Ding 2004). S1 changes more impulsively and rapidly than S2 as disclosed by the impulsive feature in their flux-curves (Fig. 4(f)).

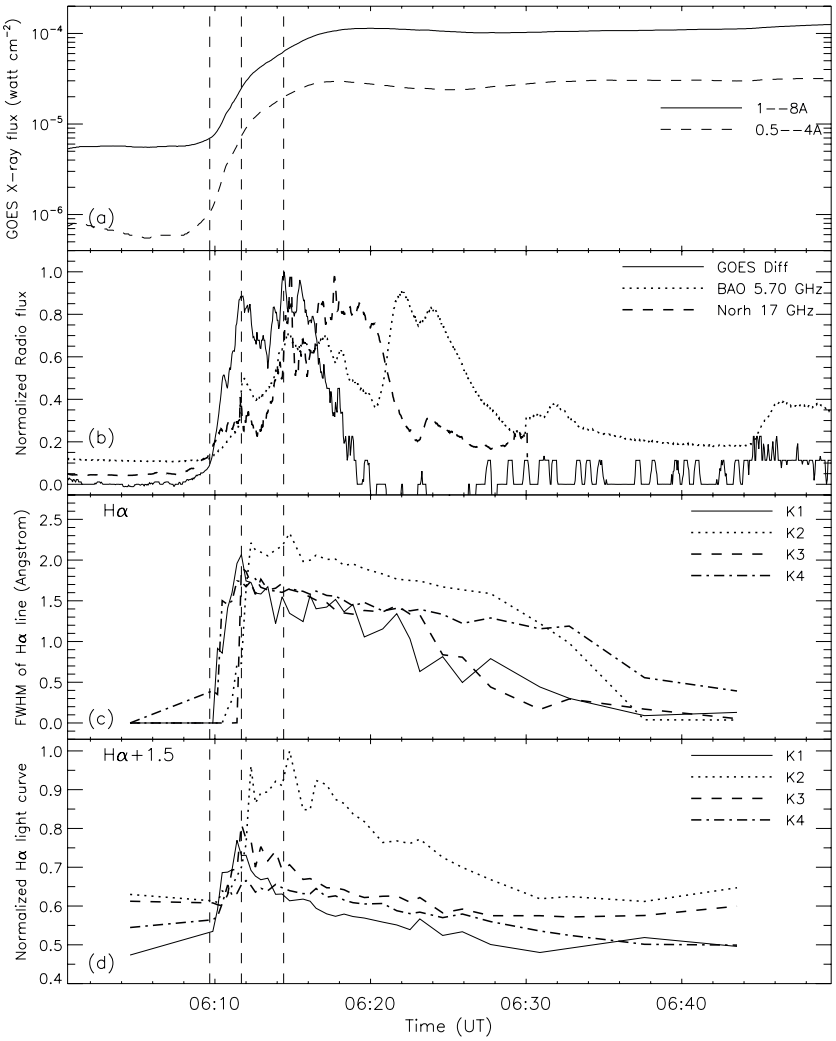

Fig. 13 (a) Time profiles of GOES X-ray flux; (b) Normalized time profiles of differential GOES X-ray flux (solid), and radio flux at 5.70 GHz from SBRS (dotted) and 17 GHz from NRO (dashed); (c) time profiles of the average FWHM of Hα line for the four selected kernels K1 (solid), K2 (dotted), K3 (dashed) and K4 (dash-dot) marked in Fig. 6; (d) same as (c) but for the brightness at Hα+1.5 Å.

Red asymmetry and red-shift were commonly observed in this flare in the Hα, the Ca II 8542 Å and the He I 10830 Å lines. The most conspicuous red asymmetry was detected in the profiles showing large emission in the far wings that we have interpreted as a signature of non-thermal particles. The derived red-shift LOS (downflow) velocities in the impulsive phase of the flare range from a few to as large as 30 km s^{-1} (Figs. 6 and 12), which is consistent with some previous results concerning the cool plasma (e.g., Wülser et al. 1994; Ding et al. 1995; Teriaca et al. 2003; Kamio et al. 2005). Ichimoto & Kurokawa (1984) and Shoji & Kurokawa (1995) measured even larger values.

Such downflows are explained by the chromospheric evaporation theory, in which explosive heating of the chromosphere to million degrees results from high-energy particles and/or thermal conduction. This theory leads to upflows of hot material and downflow motions of the cool plasma in the impulsive phase (e.g., Fisher 1987, 1989). In the later phase of the flare the values of the velocity are more uncertain because the bisector method is not well adapted to derive small velocities. A complete non-LTE computation should be applied to the Hα profiles as it was done for another flare (Berlicki et al. 2005).

The 2D distributions of the LOS velocities and the FWHMs provide for us useful information on the non-thermal electrons produced by magnetic reconnection in the corona and so are valuable diagnostic tools for the analysis of flares. The LOS velocities and the FWHMs deduced from different line profiles show similar distribution features in our case (Fig. 6), and indicate that there exist at least two magnetic reconnection processes around 06:11:42 UT and 06:14:48 UT, respectively. The first process deposited its energy mainly at kernel K3, while the second mainly at kernel K2. The outer edges of the bright kernels map the newly formed magnetic loops through magnetic reconnection. So the fact that both the maximum values of the LOS velocities and FWHMs are located on the outer edges suggests that magnetic reconnection is continually occurring, which is consistent with the scenario of two-ribbon flare models, first proposed by Kopp & Pneuman (1976), later developed by Forbes & Malherbe (1986) and generalized by Shibata (1999) and Lin & Forbes (2000). Zhao & Fang (1997), and Zhao et al. (1997) found similar results. Therefore, it can be regarded as a chromospheric piece of evidence for magnetic reconnection in solar flares.

Comparison between the differential GOES X-ray flux and the microwave flux-curves reveals a marked Neupert effect (Neupert 1968), i.e., a good correlation between these curves. Meanwhile, correlations also exist between the microwave/radio flux curves and the time profiles of the Hα FWHMs (Fig. 13(c)) and brightness at Hα+1.5 Å (Fig. 13(d)) for the four kernels, which could be an indicator of the presence of non-thermal electrons. The time profiles show that the Hα FWHMs, the LOS velocities and the Hα+1.5 Å brightness in K1 changed simultaneously with those in K4, while K2 did the same with K3.

We did not find any corresponding radio sources in the NoRH 17 GHz and 34 GHz images for kernels K2 and K3, which are also possible precipitating sites of non-thermal electrons as the optical spectroscopic observations indicate. The absence of the 17 GHz and the 34 GHz radio sources at kernels K2 and K3 is probably because the electrons deposited there had less energy than was required for emission at these frequencies (>100 keV). In contrast, radio sources were observed at kernels K1 and K4 (cf. Figs. 3 and 4). Considering the time profiles mentioned above, we infer that K1 and K4 are one pair of conjugate footpoints, while K2 and K3 are another pair.

The TRACE 195 Å images and movies show long loops connecting K1 and K4, while K2 and K3 are connected by shorter and less sheared loops. We speculate that kernels K1 and K4 are due to one magnetic process in the high-lying loop system, which released most of the energy in the flare and accelerated electrons to well above 100 keV; while K2 and K3 are due to another process following the previous one in the low-lying loop system, which released less energy and resulted in less energetic electrons. These speculations may explain the differences among the four kernels mentioned above, and are supported by the Hα flare evolution, the time profiles and the spectroscopic properties discussed in Sect. 3.3.

The three studied spectral lines – Hα, Ca II 8542 Å and He I 10830 Å – respond differently to non-thermal electron bombardment. As predicted by non-LTE calculations and observed previously, the Hα profiles show broad non-Gaussian wings and strong central reversals in the presence of non-thermal electrons, while the Ca II 8542 Å profiles are much less affected (Figs. 10 and 11). Nevertheless, the observed He I 10830 Å profiles are different. Theoretical

computation revealed that non-thermal electron bombardment increases the He I 10830 Å line strength significantly and its width moderately so that the I_{12} and I_3 components are well separated (Ding et al. 2005). In the observed profiles, these components are completely mixed together, and thus are not distinguishable. This difference may be related to the neglect of macroscopic motion in the non-LTE computation. Our observed He I 10830 Å profiles provide some constraints on the future theoretical computation of this line.

In summary, we determined two pairs of conjugate kernels in the Hα images, and their outer edges are the locations of non-thermal electron precipitation, which is demonstrated by the EUV loops and the 2D distributions of the LOS velocities and the FWHMs derived from optical spectroscopic observation. Chromospheric lines commonly present red asymmetry and red-shift in the impulsive phase of the flare, which are ascribed to the chromospheric condensation due to rapid chromospheric heating. The Hα and the Ca II 8542 Å line profiles in the impulsive phase are similar to the theoretical profiles deduced from the non-LTE computations of the non-thermal electron bombardment, while the He I 10830 Å profiles are different from the calculated ones, presumably indicating that more accurate and rigorous investigations are needed.

Acknowledgements SOHO is a joint project of ESA and NASA. We thank the NoRH staff for kindly providing the NoRH data and colleagues at HSOS for the SBRS data. This work was supported by the National Natural Science Foundation of China (NSFC, Grants 10273023, 10025315, 10221001, 10403003 and 10333040), the National Basic Research Priorities Project (G2000078402) of China, and partially by the French-Chinese contract (CNRS-CAS No. 16304). This work of BS and AB was supported by the European Commission through the RTN programme (European Solar Magnetism Network, contract HPRN-CT-2002-00313).

References

Antonucci E., Gabriel A. H., Dennis B. R., 1984, ApJ, 287, 917
Berlicki A., Heinzel P., Schmieder B. et al., 2005, A&A, 430, 679
Brown J. C., 1971, Solar Phys., 18, 489
Brown J. C., Melrose D. B., Spicer D. S., 1979, ApJ, 228, 592
Canfield R. C., Gunkler T. A., Ricchiazzi P. J., 1984, ApJ, 282, 296
Canfield R. C., Kiplingr A. L., Penn M. J. et al., 1990, ApJ, 363, 318
Carmichael H., 1964, In: W. N. Hess, ed., Physics of Solar Flares, Washington DC: NASA, p.451
David K. H., 1961, ZAp, 53, 37
Ding M. D., Fang C., Huang, Y. R., 1995, Solar Phys., 158, 81
Ding M. D., Fang C., Yin S. Y., Chen, P. F., 1999, A&A, 348, L29
Ding M. D., Chen Q. R., Li J. P., Chen P. F., 2003, ApJ, 598, 683
Ding M. D., Li H., Fang C., 2005, A&A, 432, 699
Domingo V., Fleck B., Poland A. I., 1995, Solar Phys., 162, 1
Falchi A., Qiu J., Cauzzi G., 1997, A&A, 328, 371
Fang C., Hénoux J.-C., Gan W. Q., 1993, A&A, 274, 917
Fang C., Hénoux J.-C., Ding M. D., 2000, A&A, 360, 702
Fisher G. H., 1987, Solar Phys., 113, 307
Fisher G. H., 1989, ApJ, 346, 1019
Fletcher L., Hudson H. S., 2001, Solar Phys., 204, 69
Forbes T. G., Malherbe J. M., 1986, In: Neidig D. F., ed., The Lower Atmosphere of Solar Flares, NSO/Sunspot, New Mexico, p.443
Forbes T. G., Isenberg P. A., 1991, ApJ, 373, 294
Forbes T. G., Acton L. W., 1996, ApJ, 459, 330
Fu Q. J., Qin Z. H., Ji H. R., Pei L. B., 1995, Solar Phys., 160, 97
Handy B. N., Acton L. W., Kankelborg C. C. et al., 1999, Solar Phys., 187, 229

Huang Y. R., Fang C., Ding M. D. et al., 1995, Solar Phys., 159, 127
Hudson H. S., 1972, Solar Phys., 24, 414
Hudson H. S., 1991, Bull. Am. Astron. Soc., 23, 1464
Ichimoto K., Kurokawa H., 1984, Solar Phys., 93, 105
Kamio S., Kurokawa H., Brooks D. H. et al., 2005, ApJ, 625, 1027
Kopp R. A., Pneuman G. W., 1976, Solar Phys., 50, 85
Li H., Fan Z. Y., You J. Q., 1999, Solar Phys., 185, 67
Li H, Sakurai T, Ichimoto K., S. Ueno, 2000, PASJ, 52, 465
Li H., You J. Q., 2001, A&A, 374, 1121
Li H., You J. Q., Wu Q. D., Yu X. F., 2002, Chin. Phys. Lett., 19, 742
Li H., Berlicki A., Schmieder B., 2005a, A&A, 438, 325
Li H., You J. Q., Du Q. S., Yu X. F., 2005b, Solar Phys., 225, 75
Li J. P., Ding M. D., 2004, ApJ, 606, 583
Lin J., 2004, Solar Phys., 219, 169
Lin J., Forbes T. G., 2000, J. Geophys. Res., 105, 2375
Lin J., Soon W., Baliunas S. L., 2003, New Astro. Rev., 47, 53
Liu Y., Ding M. D. 2002, ChJAA, 2, 277
Litvinenko Y. E., 1996, ApJ, 462, 997
Linsky J. L., Teske R. G., Wilkinson C. W., 1970, Solar Phys., 11, 374
Masuda S., Kosugi T., Hara H. et al., 1994, Nature, 371, 495
Melrose D. B., White S. M., 1979, Proc. Astron. Soc. Australia, 3, 369
Miller J. A., Cargill P. J., Emslie A. G. et al., 1997, JGR, 102, 14631
Miyagoshi T., Yokoyama T., 2004, ApJ, 614, 1042
Nakajima H. et al., 1994, Proc. IEEE, 82, 705
Ning Z. J., Ding M. D., Li J. P. et al., 2005, Chin. J. Astron. Astrophys., submitted
Neupert W. M., 1968, ApJ, 153, L59
Priest E. R., Forbes T. G., 2002, A&ARv, 10, 313
Qiu K. P., YeH C. T., Zhou G. P. et al., 2005, Chin. J. Astron. Astrophys., submitted
Sakao T., Kosugi T., Masuda S. et al., 1996, Adv. Space Res., 17, 67
Schmieder B., Forbes T. G., Malherbe J. M., Machado M. E., 1987, ApJ, 317, 956
Schmieder B., Malherbe J. M., Simnett G. M. et al., 1990, ApJ, 356, 720
Shibata K., 1999, Astrophys. Space Sci., 264, 129
Shoji M., Kurokawa H., 1995, PASJ, 47, 239
Sui L., Gordon H. D., 2003, ApJ, 596, L251
Sui L., Gordon H. D., Dennis B. R., 2003, ApJ, 612, 546
Švestka Z., Cliver, E. W., 1992, In: Švestka Z. et al. eds., Eruptive Solar Flares, New York: Springer-Verlag, p.1
Tang F., 1983, Solar Phys., 83, 15
Teriaca L., Falchi A., Cauzzi G. et al., 2003, ApJ, 588, 596
Tsuneta S., Hara H., Shimizu T. et al., 1992, PASJ, 44, L63
Veronig A. M., Brown J. C., Dennis B. R. et al., 2005, ApJ, 621, 482
Wülser J.-P., Zarro D. M., Canfield R. C., 1992, ApJ, 384, 341
Wülser J.-P., Canfield R. C., Acton L. W. et al., 1994, ApJ, 424, 459
Yokoyama T., Shibata K., 2001, 549, 1160
You J. Q., Wang C. J., Fan Z. Y., 1993, In: Ai G. X. et al., eds., Proceedings of the First China–Japan Seminar on Solar Physics, Kunming TonDar Institute, p.148
You J. Q., Wang C. J., Fan Z. Y., Li H., 1998, Solar Phys., 182, 431
Zhao J. W., Fang C., 1997, Chin. Sci. Bull., 42, 832
Zhao J. W., Fang C., Ding M. D., 1997, Solar Phys., 173, 121